PAPER

Check for updates

A novel multimodal nanoplatform for targeting tumor necrosis†

Xiangjun Han, [a] Oleh Taratula, [b] Anna St Lorenz, [b] Abraham S. Moses, [b] Hassan A. Albarqi, [b] Younes Jahangiri, [c] Qirun Wu, [a] Ke Xu, *[a] Olena Taratula *[b] and Khashayar Farsad *[c]

Peri-necrotic tumor regions have been found to be a source of cancer stem cells (CSC), important in tumor recurrence. Necrotic and peri-necrotic tumor zones have poor vascular supply, limiting effective exposure to systemically administered therapeutics. Therefore, there is a critical need to develop agents that can effectively target these relatively protected tumor areas. We have developed a multi-property nanoplatform with necrosis avidity, fluorescence imaging and X-ray tracking capabilities to evaluate its feasibility for therapeutic drug delivery. The developed nanoparticle consists of three elements: poly(ethylene glycol)-*block*-poly(ε-caprolactone) as the biodegradable carrier; hypericin as a natural compound with fluorescence and necrosis avidity; and gold nanoparticles for X-ray tracking. This reproducible nanoparticle has a hydrodynamic size of 103.9 ± 1.7 nm with a uniform spherical morphology (polydispersity index = 0.12). The nanoparticle shows safety with systemic administration and a stable 30 day profile. Intravenous nanoparticle injection into a subcutaneous tumor-bearing mouse and intra-arterial nanoparticle injection into rabbits bearing VX2 orthotopic liver tumors resulted in fluorescence and X-ray attenuation within the tumors. In addition, *ex vivo* and histological analysis confirmed the accumulation of hypericin and gold in areas of necrosis and peri-necrosis. This nanoplatform, therefore, has the potential to enhance putative therapeutic drug delivery to necrotic and peri-necrotic areas, and may also have an application for monitoring early response to anti-tumor therapies.

Introduction

Despite the extensive effort in cancer-related research, major scientific unknowns remain in clinically significant processes such as metastasis, therapeutic resistance, and recurrence.[1] Cancer stem cells are a group of self-renewing, multi-potential cells thought to be responsible for tumor initiation, metastasis, therapeutic resistance, and recurrence.[2] Residual tumor cells can be another source of tumor recurrence after treatment.[3,4] Cancer stem cells and residual tumor cells have been observed in peri-necrotic tumor areas,[5] a relatively protected location difficult to treat secondary to poor blood supply and possibly higher interstitial tumor pressures.[6,7] Thus, there is an unmet need to develop an effective delivery platform for therapeutic drugs to peri-necrotic and necrotic tumor zones.

Hypericin is a natural small molecule compound with intrinsic necrosis affinity.[8] Hypericin has been shown to localize with up to 17-fold higher distribution in necrotic compared with non-necrotic tissue *in vivo*.[9,10] Although the mechanism of hypericin necrosis affinity is still under investigation, its putative applications in medicine have increasingly gained attention. This includes the development of necrosis-avid contrast agents (NACA) and necrosis targeted radiotherapy.[11,12] Based on previous results, hypericin may enable drug delivery to these challenging necrotic and peri-necrotic tumor zones. However, translation of hypericin to clinical applications has been limited by its hydrophobic property and tendency to aggregate in physiological solutions. Currently, experimental uses of hypericin compounds have incorporated dimethyl sulfoxide (DMSO), polyethylene glycol (PEG) 400 and propylene glycol for delivery,[13,14] but these solvents also involve significant systemic toxicity. Improving the bioavailability and therapeutic profile of hypericin, therefore, will be of great value.

Gold is a biocompatible element with X-ray absorption and has been investigated as a computed tomography (CT) contrast agent.[15] Gold nanoparticles also have been used in molecular and cellular tracking and imaging.[16] We describe the

[a]Department of Radiology, First Hospital of China Medical University, Shenyang, Liaoning, 110001, P. R. China. E-mail: kxu@cmu.edu.cn

[b]Department of Pharmaceutical Sciences, College of Pharmacy, Oregon State University, Portland, Oregon 97201, USA. E-mail: olena.taratula@oregonstate.edu

[c]Dotter Department of Interventional Radiology, Oregon Health and Science University, Portland, Oregon 97239-3011, USA. E-mail: farsad@ohsu.edu

† Electronic supplementary information (ESI) available: Stability evaluation of Au-Hyp-NP after a month storage, safety evaluation *in vitro* and *in vivo*, fluorescence of substrates and Au-Hyp-NP, cell debris and its fluorescence, CT and DSA imaging of rabbit VX2 liver tumor. See DOI: 10.1039/d1ra05658a

development of a multimodal nano-agent delivery system based on (1) hypericin for necrosis targeting and fluorescence imaging, and (2) gold nanoparticles for fluoroscopy and CT tracking. Therefore, the developed nanoplatform can be detected by multiple imaging modalities to evaluate targeting efficiency. The novel nanostructure is constructed using a biodegradable poly(ethylene glycol)-*block*-poly(ε-caprolactone) (PEG-PCL) shell to improve aqueous solubility of inner hydrophobic cargo and thus avoid the safety concerns of using organic solvents for delivery,[17] and encapsulate hypericin and gold to enable necrosis targeting, multiple imaging and tracking capabilities. We examined nanoparticle stability, X-ray attenuation, and necrosis targeting ability using *in vitro* assays. We further observed *in vivo* tumor uptake by fluorescence and X-ray imaging. *Ex vivo* tumor evaluation demonstrated nanoparticle concentration in necrotic and pre-necrotic areas.

Results and discussion

Metastasis, therapeutic resistance, and recurrence are significant negative prognostic features in cancer.[1] These features may be due to tumor heterogeneity, possibly from stem-like cancer cells.[2] Cancer stem cells may be relatively protected by their location in tumor areas with poor blood supply, such as in peri-necrotic regions.[5] As therapeutic vehicles, nanoparticles have advantages, including passive and active targeting strategies, with additional functionality to influence the solubility, biocompatibility, and stability of therapeutic drugs.[18,19] We previously developed nanoparticles with encapsulated hypericin to facilitate necrosis targeting.[20] We have now additionally developed this nanoplatform to also include encapsulated gold for nanoplatform tracking to evaluate putative therapeutic drug delivery efficacy.

Synthesis of Au-Hyp-NP

Scheme 1 shows the composition of multimodal polymeric nanoparticles (Au-Hyp-NP). The PEG-PCL polymeric nanoparticle was loaded with (a) hypericin for necrosis targeting and fluorescence imaging,[9] and (b) gold nanoparticles for X-ray tracking properties.[21] The hydrophobicity of hypericin limits its clinical application due to its poor water solubility.[22,23] Self-aggregation of hypericin in circulation creates large clusters that can impact biological function, as well as hypericin distribution and clearance.[24,25] Large hypericin aggregates have been observed in mononuclear phagocyte system (MPS) organs leading to slow clearance. Moreover, non-aggregated hypericin formulations have been shown to have significantly improved necrosis affinity *in vivo* compared with hypericin aggregates.[10] In order to improve hypericin biodistribution for use in necrosis affinity, a variety of delivery methods have been used in previous studies, including solubilizing in organic solvents such as DMSO, or admixture with PEG 400, propylene glycol, and sodium cholate.[26,27] We incorporated a biodegradable PEG-PCL polymer shell to produce a highly biocompatible and soluble nanoplatform encapsulating gold nanoparticles and hypericin. PEG-PCL involves di-block copolymers with both hydrophilic
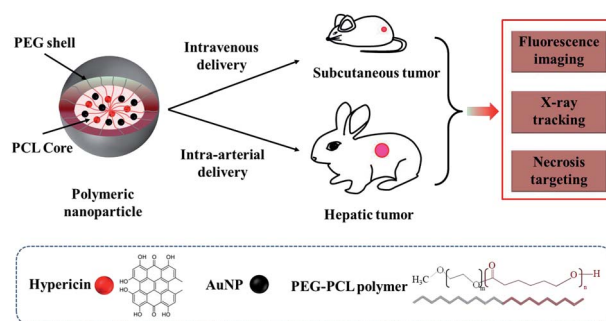
Scheme 1 Schematic illustration of multi-modality Au-Hyp-NP designed for tumor necrosis targeting. Cancer stem cells and residual tumor cells located in tumor necrotic and peri-necrotic zones are difficult to treat. A necrosis targeting nanoplatform can potentially solve this problem. The nanoplatform was developed by encapsulation of gold nanoparticles and hypericin into PEG-PCL nanoparticles. Gold nanoparticles enable X-ray tracking, and hypericin enables necrosis affinity and fluorescence imaging. *In vivo*, nanoparticles accumulated in tumor *via* passive targeting, and concentrated in areas of necrosis both *via* intravenous delivery and intra-arterial delivery. Nanoparticles were successfully monitored by fluorescence and X-ray imaging.

and hydrophobic components capable of generating water-soluble nanoparticles with a hydrophobic core and hydrophilic shell in aqueous solutions.[28] As a result, hydrophobic cargo can be encapsulated in the core, remain non-aggregated and become soluble in aqueous solution. The synthesis method we used incorporates an established emulsion solvent evaporation technique.[29,30] After solubilizing hypericin, gold nanoparticles and PEG-PCL in THF, 5% dextrose solution was added to produce an emulsion, and nanoparticles were formed after THF evaporation.

Characterization

The hydrodynamic size of the Au-Hyp-NPs was 103.9 ± 1.7 nm with a polydispersity index (PDI) of 0.12 ± 0.02 from DLS analysis (Fig. 1A). PDI values of less than 0.2 indicate a monodisperse size distribution of nanoparticles. By dark-field microscopy, nanoparticles showed good dispersity and spherical shape (Fig. 1C). Cryo-TEM images revealed a high density of gold nanoparticles aggregated within PEG-PCL (Fig. 1D). Based on a zeta potential of -17.3 ± 4.1 mV, the negative charge of the Au-Hyp-NPs was likely due to the incorporation of gold nanoparticles, as the zeta potential of gold nanoparticles alone is approximately -20 mV.[31,32] The composition of Au-Hyp-NP was analyzed *via* UV-Vis spectroscopy. Nanoparticles demonstrated the specific absorption peaks of hypericin and the slope for gold nanoparticles (Fig. 1B). The two specific absorption peaks of hypericin in THF were 599.5 and 554 nm, and the corresponding peaks in Au-Hyp-NP were 597 nm and 553 nm. The absorption peaks were slightly blue-shifted, most probably due to encapsulation within a PEG-PCL shell. At 525 nm, there was a very low absorption of hypericin and high absorption of gold nanoparticles, therefore, absorption peaks at 525 and 600 nm were used to create standard calibration curves for gold nanoparticles and hypericin. According to peak absorption
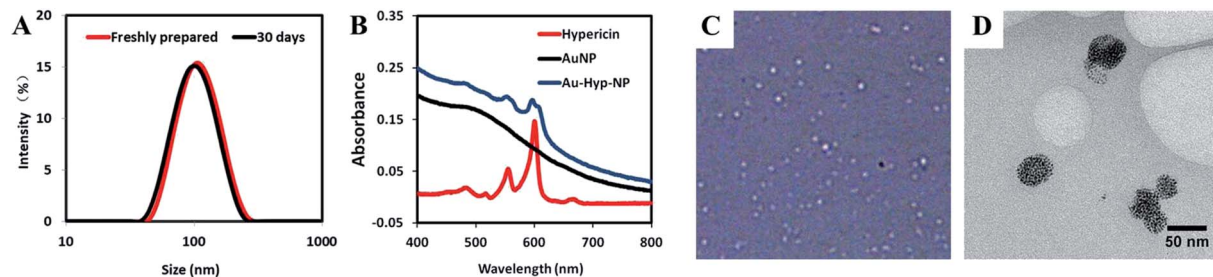
Fig. 1 Characteristics of Au-Hyp-NP. (A) Size distribution of Au-Hyp-NP measured by dynamic light scattering before and after 30 days preserved at 4 °C. (B) UV-Vis absorption spectra of the Au-Hyp-NP, gold nanoparticles and hypericin demonstrate nanoparticles containing the specific absorption peaks of hypericin and the slope of gold nanoparticles (gold concentration of 35.7 µg mL^{-1}). (C) Nanoparticle morphology by dark field microscopy (magnification ×1000). (D) Morphology of Au-Hyp-NP examined by cryo-TEM (the scale bar is 50 nm, magnification ×68 000).

measurements, the formulated nanoparticles contained 713.2 µg mL^{-1} of gold and 46.7 µg mL^{-1} of hypericin, resulting in an encapsulation efficiency of 71.3% gold and 93.4% hypericin.

Stability evaluation of the nanoparticles revealed no significant changes in nanoparticle size distribution or zeta potential over a period of thirty days in aqueous solution at 4 °C (Fig. 1A and Table S1†), with only 10.4% of gold nanoparticles and 8.8% of hypericin released from the nanoparticles (Fig. S1†). This indicates that the nanoplatform is stable for potential future translational applications. However, interactions among
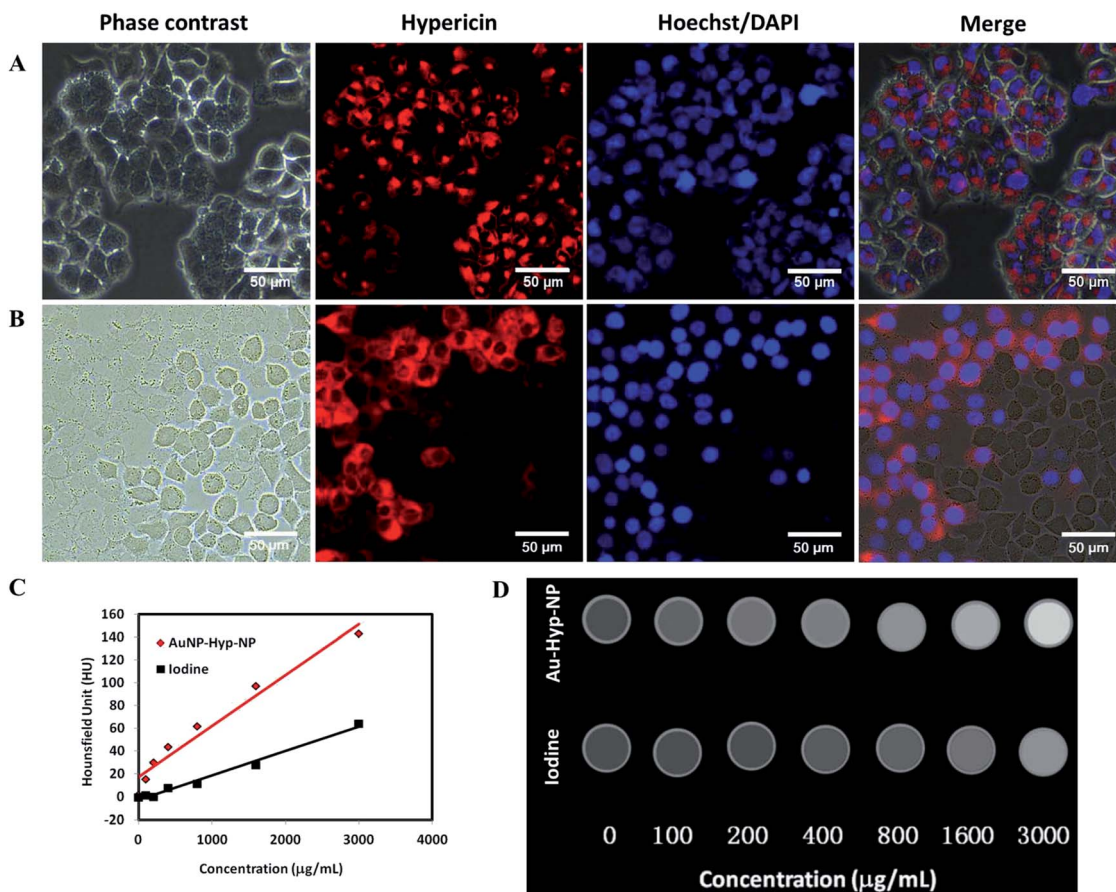

Fig. 2 Fluorescence imaging, X-ray imaging and necrosis targeting evaluation of Au-Hyp-NP *in vitro*. (A) Fluorescence microscopy images of A2780 ovarian cancer cells incubated with Au-Hyp-NP with hypericin concentration of 7.0 µg mL^{-1} for 24 h. Hoechst stain for nuclei and hypericin fluorescence localized in cytoplasm. (B) The necrosis affinity of Au-Hyp-NP in A2780 cells by dry ice cryo-death assay. Cell death was induced by applying 1 cm dry ice directly under the culture well with confluent A2780 cells, and nanoparticles with hypericin concentration of 7.0 µg mL^{-1} were incubated for 15 min (left portion of the field without visible cell contours represents dead cells). Hypericin distribution by red fluorescence in dead cells colocalizes to DAPI for cell nuclei in permeabilized dead cells (the scale bar is 50 µm). (C) CT imaging of Au-Hyp-NP examined by micro-CT with different concentrations, using iohexol with different iodine concentrations as the control. (D) CT images of Au-Hyp-NP and iohexol at different concentrations respectively (0–3000 µg mL^{-1}). Window width = 330 HU, window center = 40 HU.

nanoparticles and various factors after intravenous injection may influence nanoparticle stability in as yet unknown ways. Potential variables that may affect *in vivo* nanoparticle dynamics include size and surface charge of nanoparticles, blood flow, type of blood cells and serum components.[33] More effort will be needed for further characterization of the nanoparticle for clinical translation in the future.

Safety evaluation *in vitro*

The hemolysis test and calcein AM assay analysis were performed to investigate the potential toxicity of the gold and hypericin-loaded polymeric nanoparticles. For hemolysis evaluation, the UV-Vis absorption of hemoglobin at 540 nm or 570 nm was used to detect hemolysis as previously described.[34,35] Due to potential overlap in absorption wavelengths of hemoglobin and hypericin, we counted the intact red blood cell number to evaluate for hemolysis. Hemolysis was not observed at gold concentrations from 500 to 62.5 $\mu g\ mL^{-1}$ of tested nanoparticle and PBS control ($p = 0.23$), and the intact red blood cell rate remained $94.4 \pm 3.3\%$ with nanoparticle gold concentrations of 500 $\mu g\ mL^{-1}$ (Fig. S2A†). Calcein AM assay analysis employed for cell safety indicated that no significant cell damage was observed with nanoparticles of gold concentration from 31.3 to 250 $\mu g\ mL^{-1}$ compared with RPMI 1640, and the cell viability decreased to $59.8 \pm 18.2\%$ at gold concentrations of 500 $\mu g\ mL^{-1}$ ($p < 0.01$) (Fig. S2B†). Both hemolysis and cytotoxicity results suggested that the PEG-PCL polymeric nanoparticles can encapsulate the hydrophobic material for suitable *in vivo* delivery. The decrease in cell viability with increasing concentrations of nanoparticles was potentially due to cytotoxic and apoptogenic effects of hypericin, as previously observed in cancer cells.[36] The other materials used, including PEG-PCL and gold, have shown no significant cytotoxicity in previous studies.[28,37]

Cellular internalization evaluation

Au-Hyp-NP retained intrinsic hypericin fluorescence after encapsulation in nanoparticles (Fig. S3†). To demonstrate the ability of nanoparticles to be taken up by tumor cells, we used A2780 ovarian cancer cells, which have been shown to take up PEG-PCL encapsulated nanoparticles in previous studies.[20,30] Incubation of A2780 cells with 7.0 $\mu g\ mL^{-1}$ hypericin in nanoparticles for 24 h demonstrated intracellular hypericin uptake by fluorescence microscopy, showing preservation of hypericin fluorescence after encapsulation within the nanoparticles (Fig. 2A). Hoechst staining showed no colocalization with the nucleus, demonstrating hypericin accumulation in the cytoplasm. To quantify nanoparticle uptake, cell lysates were analyzed by spectrophotometry. Quantitative measurement of compounds in solution demonstrated at least 0.012 ± 0.003 pg hypericin uptake per cell, although this is likely an underestimate due to significant residual hypericin remaining in the cell debris pellet (Fig. S4†), presumably due to hydrophobic interactions with denatured proteins. Cellular internalization of Au-Hyp-NP thus retained its fluorescence imaging ability.

In vitro cell death assay

A dead cell assay with cultured cells exposed to dry ice, previously used to investigate necrosis affinity of compounds,[20,38] was employed to test the necrosis affinity of Au-Hyp-NP nanoparticles (Fig. 2B). We used DAPI to assess the cell permeation and nuclear staining in this assay, since DAPI does not acutely penetrate viable cells with intact cell membranes. After staining with DAPI for 5 min, DAPI localization was seen in dead cells exposed to dry ice, with colocalization of hypericin fluorescence. This assay suggests that while Au-Hyp-NP can localize in the cytoplasm of intact cells, in the presence of dead cells, nearly all nanoparticles accumulated in the dead zone. Moreover, dead cells showed greater and faster Au-Hyp-NPs accumulation than intact cells (15 min *vs.* 24 h). Of note, this experiment also showed that encapsulation of hypericin in a PEG-PCL shell was able to preserve its necrosis affinity. While the mechanism of hypericin necrosis affinity is not well understood, one hypothesis involves loss of cell membrane integrity during necrosis with intracellular penetration, potentially through hydrophobic interactions with specific molecules or phospholipids.[38,39]

X-ray attenuation evaluation

CT imaging is based on X-ray attenuation. Advantages of CT imaging include fast examination speed, high spatial resolution, deep penetration, relatively low cost, and the capability of quantitative analysis and *in vivo* real-time acquisition.[40] With micro-CT analysis, the developed nanoparticles demonstrated greater relative CT attenuation than a standard intravenous iodinated contrast agent, iohexol, at similar concentrations (Fig. 2C). Fig. 2D shows CT images of polymeric nanoparticles and iohexol at increasing concentrations (0–3000 $\mu g\ mL^{-1}$). Nanoparticle uptake, based on X-ray attenuation using Hounsfield Units (HU), was quantified. A linear increase in attenuation was observed with increasing nanoparticle concentrations, and with greater relative attenuation compared with iohexol. This supports the potential for this nanoplatform for *in vivo* tracking and biodistribution analysis at a clinically meaningful range.

Fluorescence and X-ray tracking *in vivo* using a nude mouse bearing A2780 tumor

Necrosis is common during tumor growth, increasing with larger tumor size due to lack of blood supply.[41] Necrosis has been observed with tumor diameters as small as 9.0 ± 0.5 mm.[42] We assessed *in vivo* nanoparticle necrosis affinity in a xenotropic mouse subcutaneous tumor model with a tumor diameter >10 mm, analysing the dual properties of fluorescence and X-ray attenuation. To evaluate the fluorescence and X-ray attenuation of Au-Hyp-NP *in vivo*, the fluorescence of hypericin and X-ray imaging of gold were monitored by IVIS (Perkin Elmer, Waltham, MA) before and after nanoparticle intravenous injection (IV) at different time points. Hypericin accumulation was observed gradually within the subcutaneous tumor, with greatest fluorescence intensity 30 minutes after nanoparticle injection (Fig. 3A). After 24 h, fluorescence decreased to background levels, revealing relatively rapid physiologic clearance.
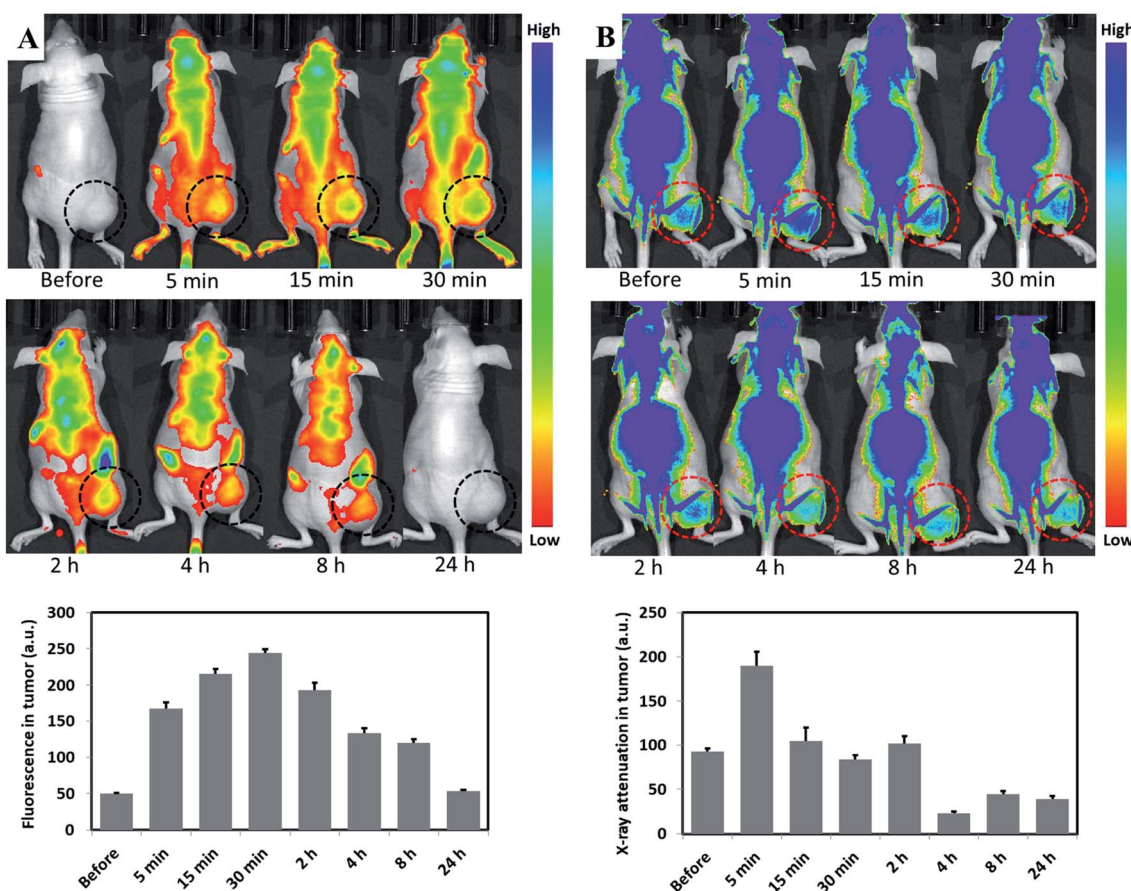
Fig. 3 Fluorescence and X-ray attenuation of Au-Hyp-NP in a nude mouse bearing A2780 subcutaneous tumor at different time points after intravenous injection (gold dose 8 mg kg^{-1}, hypericin dose 0.6 mg kg^{-1}): before injection, and at 5 min, 15 min, 30 min, 2 h, 4 h, 8 h, 24 h post-injection. (A) Fluorescence images, (B) X-ray attenuation images. Images obtained on IVIS Lumina XRMS series III system. The circle indicates tumor location. The first image in (B) shows the intrinsic X-ray attenuation of the mouse and tumor without nanoparticles.

In vivo X-ray attenuation of gold was also observed, reaching the highest density 5 minutes after nanoparticle injection, and gradually decreasing to baseline levels 2 h after injection (Fig. 3B). These results suggest that the fluorescence imaging and X-ray tracking properties of the developed nanoparticles can be employed qualitatively *in vivo*; however, due to the limited penetration depth of fluorescence and nanoparticle accumulation in deep tissues and organs, quantitative analysis of nanoparticle biodistribution in this model is presently challenging. The rapid clearance results within 24 h also demonstrated that, although hypericin and gold are not biodegradable, encapsulation into nanoparticles with a PEG-PCL shell conferred relative biocompatibility with lack of retention in non-target organs. Interestingly, the time point of greatest fluorescence intensity was later than the time point of highest X-ray attenuation. This may be due to intratumoral PEG-PCL nanoparticle degradation.[20] We hypothesize that after exposure to extracellular cytosolic compounds in necrotic tissue, PEG-PCL nanoparticles were disrupted, resulting in relatively greater hypericin retention, possibly in necrotic tissue for its necrosis affinity, and earlier clearance of free gold resulting in a relatively later peak fluorescence signal compared with X-ray attenuation.

CT tracking *in vivo* using rabbit VX2 liver tumor *via* nanoparticles intra-arterial injection (IA)

To investigate the CT tracking capability of Au-Hyp-NP through intra-arterial injection, a well-established rabbit VX2 orthotopic liver tumor model was employed in three rabbits.[43] The VX2 model has been used to study transarterial liver-directed therapy, clinically used to treat hepatocellular carcinoma and liver metastases.[44,45] After injection of Au-Hyp-NP at a gold dose of 1.5 mg kg^{-1}, CT imaging was performed before and after nanoparticle injection at different time points. Fig. 4 demonstrated nanoparticle accumulation rapidly into the tumor and showed peak lesion attenuation 5 min after nanoparticle injection. This result suggests Au-Hyp-NP can be monitored *in vivo* by CT imaging, and the nanoplatform has the potential to delivery putative drug to tumor.

Ex vivo analysis of hypericin and gold distribution

To assess the distribution of nanoparticles in organs *in vivo*, organs including brain, heart, lung, liver, spleen, kidney and tumor were harvested in the treated mouse for fluorescence observation on the Pearl Imaging System with a 700 nm channel. Au-Hyp-NP predominantly accumulated in the tumor, and followed by the liver and kidney (Fig. 5).
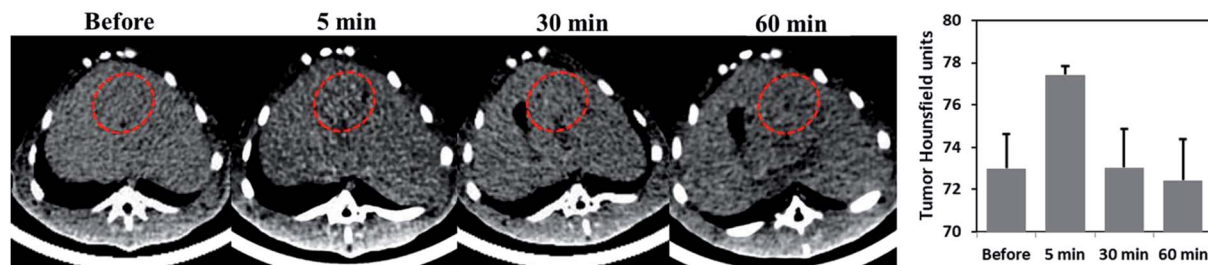
Fig. 4 CT tracking of Au-Hyp-NP in rabbit VX2 liver tumor at different time points after intra-arterial injection (gold dose 1.5 mg kg^{-1}). CT scanning time points include before injection, and at 5 min, 30 min, 60 min post-injection. CT values in tumor showed the highest attenuation (Hounsfield units) at 5 min after Au-Hyp-NP injection ($p = 0.04$). The red circle indicates tumor location. This suggests the Au-Hyp-NP nanoplatform could be monitored by CT imaging *in vivo*.
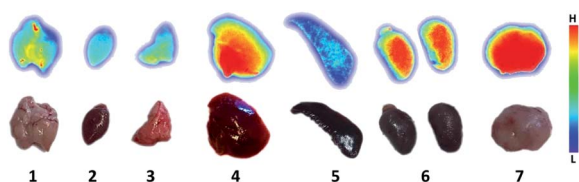

Fig. 5 Au-Hyp-NP distribution in different organs obtained on the Pearl Imaging System with a 700 nm channel. Organs were harvested 30 min after intravenous injection in the treated mouse, including 1 (brain), 2 (heart), 3 (lung), 4 (liver), 5 (spleen), 6 (kidney), 7 (tumor).
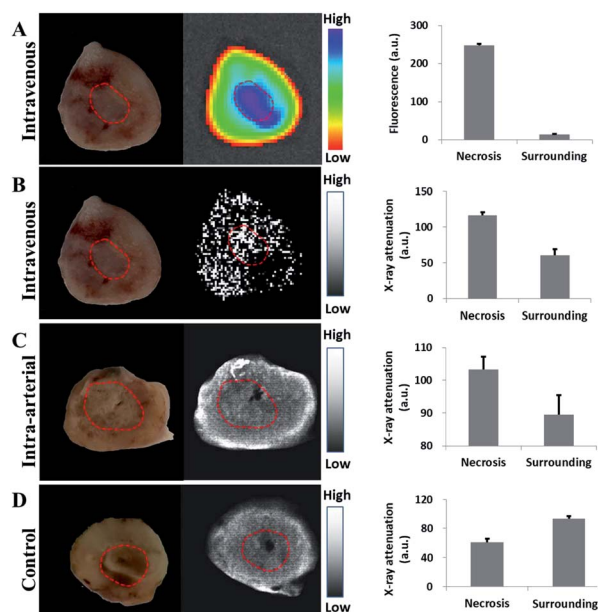

Fig. 6 Tumor slice and the associated fluorescence and X-ray attenuation images. (A) Fluorescence image of tumor 30 min after IV nanoparticle injection (gold dose 8 mg kg^{-1}, hypericin dose 0.6 mg kg^{-1}). (B) X-ray attenuation images with Au-Hyp-NP IV nanoparticle injection. Tumor images in (A) and (B) were obtained on an IVIS Lumina XRMS series III system. (C) X-ray attenuation images with Au-Hyp-NP IA nanoparticle injection (gold dose 1.5 mg kg^{-1}). (D) Control with saline injection. (C) and (D) were obtained using a mammography imaging system. The red circle indicates necrotic area in the tumor. Bars represent the mean and standard deviation of three measurements for each condition.

To assess the feasibility of necrosis affinity *in vivo*, tumor slices with grossly visible central necrosis were cut to detect the distribution of hypericin by fluorescence intensity and gold by X-ray attenuation. Thirty minutes after intravenous injection of Au-Hyp-NP in a mouse bearing a subcutaneous ovarian cancer tumor, a 2 mm tumor slice was obtained. The highest fluorescence intensity of hypericin was observed in the center of the tumor in the area of gross necrosis (Fig. 6A). Necrotic tissue typically demonstrates lower X-ray attenuation than the surrounding soft tissue due to cell structure lysis.[46] After intravenous nanoparticle injection, however, there was greater X-ray attenuation in the tumor center in the region of necrosis (Fig. 6B) consistent with nanoparticle accumulation. A 3 mm rabbit VX2 liver tumor slice obtained five minutes after intra-arterial injection of Au-Hyp-NP also demonstrated similar results, with higher X-ray attenuation in the necrotic zone compared with that in the control sample without nanoparticle injection (Fig. 6C and D).

These proof-of-concept fluorescence and X-ray attenuation results demonstrated that PEG-PCL nanoparticles encapsulating hypericin and gold not only target tumor tissue, but also concentrate within necrotic tumor tissue *in vivo*.

Histologic analysis

To investigate hypericin necrosis affinity using this nanoplatform, morphological changes and fluorescence distribution were evaluated in tumor sections by histology (Fig. 7). Tumor sections from the injected mouse and rabbits revealed similar
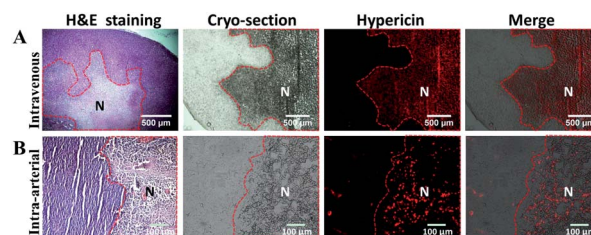

Fig. 7 Histological analysis of hypericin distribution. Hypericin fluorescence distribution co-localized to necrotic zones as indicated by H&E staining and cryo-section. (A) A2780 tumor slices were harvested 30 min after IV nanoparticle injection (the scale bar is 500 μm). (B) VX2 orthotopic liver tumor slices were harvested 5 min after IA nanoparticle injection (the scale bar is 100 μm). "N" indicates necrotic area in tumor.

results. H&E staining and cryo-sections demonstrated central necrosis in the tumors, with loss of tumor cell membranes and intracellular organelles. Fluorescence imaging revealed the distribution of hypericin from the nanoparticles coinciding with the areas of necrosis.

To investigate gold distribution, TEM was performed in tumor samples 5 min after IA nanoparticle injection. In order to obtain images of gold nanoparticles within the tissue without artifact, the peri-necrotic and necrotic portions of the tumor were processed according to protocol but without uranium citrate and lead acetate staining, 70–90 nm slices were cut and observed on TEM.[47] In the peri-necrotic zones, gold accumulation was observed in intracellular substructures, possibly putative lysosomes of viable cells (Fig. 8A). In the necrotic zones, cells were significantly smaller with loss of intrinsic cell structure, and gold was diffusely observed (Fig. 8B). These results show Au-Hyp-NP may partially localize in lysosomes in viable cells, and suggest a putative pathway for intracellular nanoparticle uptake and degradation. In necrotic tissue, extracellular lysosomal materials and denatured proteins may penetrate the nanoplatform and result in more diffuse degradation and localization of nanoparticle products. The lysosomal pathway may thus represent an intriguing mechanism for Au-Hyp-NP internalization and degradation for effective delivery to peri-necrotic and necrotic zones. Confirmation of this will require further study.

Our nanoplatform was developed using amphiphilic PEG-PCL polymeric materials to simultaneously encapsulate both hypericin and gold. The hydrophilic property of the PEG layer provides safety and solubility in aqueous solution. PEG also provides stability and control of surface properties. PEG chains and structure may play a role in tissue targeting ability, including lymph nodes, muscle, liver, spleen, and kidney.[48] The hydrophobic property of the PCL layer enables encapsulation and delivery of hydrophobic agents. Thus, hydrophobic hypericin and gold nanoparticles both packed within the core of the PEG-PCL platform (as shown in Fig. 1D). The *ex vivo* and histological analysis demonstrated successful necrosis targeting ability of Au-Hyp-NPs. Free hypericin is not soluble and easily aggregates in circulation, which is then rapidly cleared by the mononuclear macrophage system. Nanoparticles can therefore prolong the encapsulated hypericin blood circulation time, enabling greater hypericin accumulation in necrotic tumor zones. At present, the enhanced permeability and retention (EPR) effect effectively allows nanoparticle accumulation to the target site; however, future iterations of the nanoplatform can facilitate modification of the PEG-PCL shell for potentially greater tissue and tumor-specific targeting. The nanoplatform proved stable in circulation, and its size greatly increased when contacted with surfactant such as 5% sodium dodecyl sulfate.[20,49] We hypothesize that due to exposure of Au-Hyp-NPs to extracellular surfactants in necrotic cells, the equilibrium for nanoparticle formation was disrupted resulting in increased nanoparticle size to expose the encapsulated hypericin. The exposed hypericin then accumulated in necrotic zones. When contacted with hydrophobic materials in necrotic tissue, Au-Hyp-NPs degraded and released both encapsulated hypericin and gold nanoparticles to the necrotic zone, enabling multimodal functionality of these agents in this region.
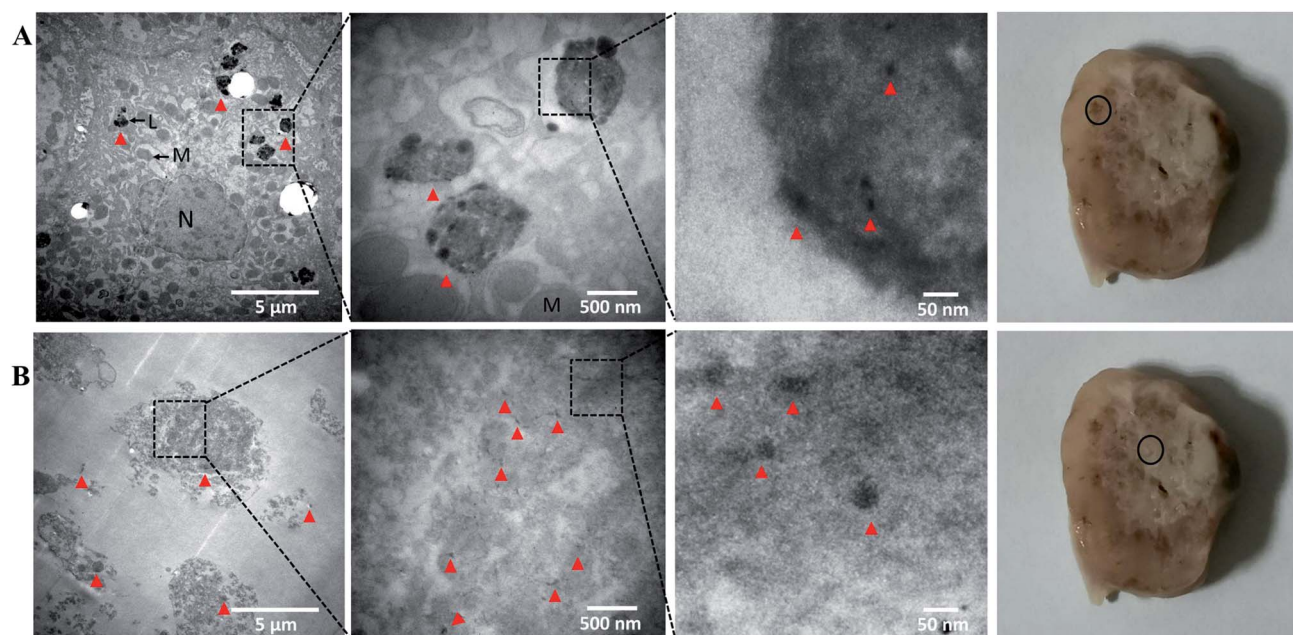

Fig. 8 Gold distribution analysis in a VX2 tumor harvested from IA nanoparticle injection in a rabbit by TEM. (A) The viable cells were obtained from the peri–necrotic zone indicated by a black circle in the gross photograph in the last column. The cells are large with intact cell membrane and organelles, and nanoparticles accumulated in putative lysosomes. (B) TEM of the necrotic zone indicated by a black circle in the gross photograph in the last column. The visible cells were small with damaged cell membranes and organelles, and nanoparticles were diffusely dispersed. "N" indicates nuclei, "M" indicates mitochondria, "L" indicates lysosome, red markers indicate nanoparticle location.

On the basis of X-ray attenuation, imaging by IVIS, mammography imaging system, CT and TEM, nanoparticle distribution was successfully tracked due to gold encapsulation. Based on the degree of signal to background, however, further optimization will be needed for this nanoplatform to serve a role as a clinical CT contrast agent. More effort will be needed in the future to facilitate this function of the nanoplatform.

Safety evaluation *in vivo*

Safety evaluation *in vivo* was evaluated using histological analysis by H&E staining between the treated mouse and an untreated control. No significant gross morphological differences were found in heart, liver, spleen, lung, kidney, brain and pancreas between the two groups (Fig. S5†).

Experimental

Materials

Hypericin from *Hypericum perforatum* was purchased from Sigma-Aldrich Co. (USA) and PEG-PCL (methoxy poly(ethylene glycol)-*b*-poly(ε-caprolactone), MW = 15 000 Da, PDI = 1.21, the MW ratio of PEG : PCL = 5000 : 10 000) from Advanced Polymer Materials Inc. (Canada). Gold nanoparticles in toluene with a concentration of 10 mg mL^{-1} (size: 2–4 nm) were purchased from Ocean Nano Tech LLC (USA). All other analytical grade reagents were obtained from Fisher Scientific, Inc. (USA) and VWR International, LLC (USA).

Preparation of gold and hypericin loaded nanoparticles (Au-Hyp-NP)

Gold nanoparticles were prepared by the following method: 2 mg gold nanoparticles in 200 μL toluene were mixed with 1 mL acetone, the solution was centrifuged at 15 000 rpm for 20 min, and the gold nanoparticles were recovered by removing the supernatant.

Polymeric nanoparticles containing gold and hypericin (Au-Hyp-NP) were prepared using the emulsion solvent evaporation method.[50] Briefly, 5 mg PEG-PCL, 100 μg hypericin and 2 mg gold nanoparticles were dissolved in 2 mL tetrahydrofuran (THF). The solution was transferred to a 15 mL tube and continuously agitated for 30 minutes. Then, 2 mL of 5% dextrose solution was added to the previous solution with agitation for an additional 30 minutes. The final solution was transferred to a 20 mL scintillation vial and left in a chemical hood overnight to evaporate residual THF under dark conditions. The final volume was adjusted to 2 mL using water, and filtered using a 0.2 μm filter to obtain the final Au-Hyp-NP nanoparticles. For CT property evaluation, nanoparticles with a higher concentration were obtained by evaporating water to decrease the final volume of solution.

Characterization

The hydrodynamic diameter, size distribution, and zeta potential of Au-Hyp-NP were determined using dynamic light scattering (DLS, Malvern ZetaSizer NanoSeries, Malvern, U.K.) according to manufacturer protocol. Briefly, 10 μL samples were diluted in 1 mL ultra-pure water and evaluated in the DLS system. All measurements were conducted at 25 °C and each parameter was recorded in triplicate.

The morphology and size of the nanoparticles were observed using an inverted optical microscope equipped with a dark-field condenser (Leica Microsystems, DM750, Leica, Switzerland) and cryogenic transmission electron microscopy (cryoTEM) according to the manufacturer protocol. For dark-field microscopy, 5 μL samples were fixed onto micro slides with a coverslip. The oil immersion objective was used to observe the sample at 1000× magnification. For cryoTEM, 4 μL samples were applied onto glow-discharged (60 s, 15 mA) 400 mesh copper grids with thin carbon film supported by a lacey carbon substrate (Ted Pella 01824). Grids were blotted for 3 s at 22 °C and 100% humidity using a blot force of −15, then plunged into liquid ethane using a Vitrobot Mark IV (FEI). Images were recorded with a K2 Summit camera (Gatan) in counting mode on a Talos Arctica microscope (FEI) operated at 200 kV. CryoTEM images were collected with a defocus range of 2–4 μm.

The composition was examined using an ultraviolet and visible spectrophotometer (UV-1800 spectrophotometer, Shimadzu, Carlsbad, CA). To assess the gold and hypericin encapsulation efficiency, the solution of prepared nanoparticles was vacuum-dried to remove water, and then re-dissolved in THF. After obtaining the standard calibration curves for gold nanoparticles and hypericin, the gold and hypericin concentration was quantified by UV-Vis absorption at 525 nm and 600 nm, respectively. The encapsulation efficiency was evaluated as the percentage of gold or hypericin weight encapsulated in nanoparticles over the initial weight of gold or hypericin used for synthesis.

The samples were stored for thirty days at 4 °C protected from light. Nanoparticles were re-evaluated for size, surface charge, hypericin, and gold encapsulation to assess stability over time.

Hemolysis evaluation

2.5% of red blood cells in PBS suspension were prepared to evaluate interaction with Au-Hyp-NP. Briefly, whole blood was obtained from swine in EDTA. Blood serum was removed after centrifugation (2000 rpm, 10 min). Red blood cells were collected by centrifugation and washed three times with PBS, and then dispersed in PBS to get 2.5% volume of red blood cells in solution. 20 μL cell dispersion was then mixed with Au-Hyp-NP diluted in PBS suspension with the gold concentration ranging from 500 to 62.5 μg mL^{-1} and hypericin concentration from 32.7 to 4.1 μg mL^{-1}. PBS without Au-Hyp-NP was used as the control. Cells were incubated for 3 h in a 37 °C water bath, then 20 μL of the mixture were pipetted to investigate the number of intact red blood cells using hemocytometer. All tests were performed in triplicate.

Cell culture and *in vivo* tumor model

Human ovarian epithelial carcinoma cells (A2780 cell line) were cultured in RPMI 1640 medium and DMEM medium with 10% FBS respectively at 37 °C with 5% CO$_2$ in a humidified

incubator. All animal studies were approved by the institutional animal care and use committee (IACUC) and all procedures were performed according to IACUC policies. Subcutaneous tumors were developed by injection of A2780 cells (2×10^6) in DMEM medium into the flank of six-week-old athymic nude mice (Charles River Laboratories, MA). One mouse with tumor was injected with the nanoparticles, the other mouse was injected with saline as a control. VX2 orthotopic liver tumors were developed in six New Zealand White rabbits by injection of small fragments of VX2 tumor into rabbit liver *via* a 17G needle under ultrasound guidance according to prior protocol.[43] Three tumor-bearing rabbits were assayed for CT tracking evaluation, one was assayed for *ex vivo* analysis, and others were used for controls. Follow-up enhanced CT (Optima CT 680, GE, USA) was performed every two weeks to monitor tumor size and location. Intrinsic tumor necrosis developed in these tumors when the longest tumor diameter was greater than 10 mm.

Cytotoxicity evaluation

A modified cell viability assay based on calcein AM (Biotium, Inc., Hayward, CA) was conducted as previously described to evaluate the potential intrinsic cytotoxicity of Au-Hyp-NP.[51] A2780 cells were seeded in a 96-well plate (10 000 cells per well) and cultured overnight to allow for cell attachment. 100 μL Au-Hyp-NP were added to the well at gold concentrations from 500 to 31.3 μg mL^{-1}. Cells incubated with RPMI 1640 medium instead of Au-Hyp-NP was the control. After 24 h culture in the dark, cell viability was assessed with calcein AM solution (10 μM in PBS solution) for 30 min. The fluorescence of each well was recorded by a multiwell Synergy HT plate reader system (BioTek Instruments, Winooski, VT) with 485/528 nm excitation/ emission filters. The cell viability (%) was expressed as a percentage relative to the control group. Experiments were performed five times each.

Cellular internalization evaluation

A2780 cancer cells were cultured using a T75 flask to 40% confluency. Au-Hyp-NPs were added to the cells with a gold concentration of 100 μg mL^{-1} and cultured 24 h in the dark. Hoechst staining was used to stain cell nuclei for 30 min according to manufacturer protocol. Consequently, cells were washed 3 times with PBS and imaged with an EVOS FL Cell Imaging System (Life Technologies, Grand Island, NY). Next, after being trypsinized and counted, all cells were lysed with 2 mg mL^{-1} NaOH solution for 30 min and further diluted in THF to dissolve hypericin (100 μL NaOH : 700 μL THF). The UV absorption of hypericin was recorded, and the uptake per cell was calculated according to the calibration standard curve. The cell debris fluorescence was investigated on the Pearl Imaging System with a 700 nm channel to evaluate the presence of residual hypericin.

In vitro cell death assay

The necrosis affinity of Au-Hyp-NP was evaluated using an *in vitro* cell death assay as previously described.[52] Briefly, A2780 cancer cells (20 000 cells per well) were seeded in a 12-well plate

and grown to confluency in RPMI-1640 medium. After removing culture medium, a 1 cm diameter piece of dry ice was applied to the underside of the culture well for 30 seconds. Then, Au-Hyp-NPs with a gold concentration of 100 μg mL^{-1} were added to the culture well for 15 min, and DAPI was used to stain cell nuclei for 5 min according to manufacturer protocol. Finally, the cells were gently washed with PBS and imaged using an EVOS FL Cell Imaging System (Life Technologies, Grand Island, NY).

CT imaging attenuation *in vitro*

CT imaging *in vitro* was performed using a MicroCT system (Inveon, Siemens). Au-Hyp-NP dispersed in water with a gold concentration ranging from 0 to 3000 μg mL^{-1} were pipetted in Eppendorf tubes and scanned by MicroCT. Iohexol contrast (Omnipaque™, GE Healthcare Inc) with iodine concentration in the same range as the nanoparticle gold concentrations was used as the control group. Scanning was performed at 80 keV voltage and 450 μA current. The CT values of each group were recorded to evaluate the CT attenuation of the nanoparticles.

Fluorescence and X-ray tracking *in vivo* using nude mice bearing A2780 tumors

To investigate the fluorescence and X-ray tracking property of Au-Hyp-NP *in vivo*, a 0.2 mL amount of Au-Hyp-NP (gold dose 8 mg kg^{-1}, hypericin dose 0.6 mg kg^{-1}) was intravenously injected *via* the tail vein into a nude mice bearing A2780 subcutaneous tumor. Fluorescence and X-ray imaging was performed using IVIS Lumina XRMS series III system (Perkin Elmer, Waltham, MA) before injection and at the following time points: 5 min, 15 min, 30 min, 2 h, 4 h, 8 h, and 24 h after injection. The fluorescence excitation wavelength of 600 nm and emission wavelength of 670 nm were used for hypericin detection. All images were processed by ImageJ software, fluorescence and X-ray attenuation in tumor zone were measured using triplicate region of interest (ROI) selection.

CT tracking *in vivo* using rabbit VX2 liver tumor *via* intra-arterial injection

To evaluate the CT tracking property of Au-Hyp-NP *via* intra-arterial injection, three rabbits bearing VX2 orthotopic liver tumors were employed.[53] After iodinated contrast-enhanced CT confirmation of tumor size over 1 cm (Fig. S6†), rabbits were prepared to conduct selective intra-arterial injection. After induction of general anesthesia with 2.5% inhalational iso-flurane, the femoral artery was exposed and a 5 F vascular sheath was inserted. Then a microcatheter (Terumo Medical Corporation, Japan) was used to selectively catheterize the proper hepatic artery under fluoroscopy. Angiography was performed to identify the characteristic tumor staining using 1 mL iohexol contrast injection (Fig. S6†). Next, the catheter was left in position and the animals were transferred to the CT scanning system. Au-Hyp-NPs were injected *via* the catheter at a gold dose of 1.5 mg kg^{-1}, then repeated CT scanning was performed to obtain the tumor images at the following time points: before injection, 5 min, 30 min, and 60 min after injection. All images

were transmitted into a picture archiving and communication system (PACS) to conduct further analysis.

Ex vivo analysis of hypericin and gold distribution

To assess the distribution of nanoparticles in organs *in vivo*, organs including brain, heart, lung, liver, spleen, kidney and tumor were harvested 30 minutes after intravenous nanoparticle injection in the treated mouse on the basis of fluorescence imaging *in vivo* results, and fluorescence were observed on the Pearl Imaging System with a 700 nm channel for hypericin evaluation.

To evaluate the hypericin and gold distribution in tumors, the mouse tumor was harvested 30 minutes after intravenous nanoparticle injection. A 2 mm slice was made across the largest part of the tumor to analyze by fluorescence and X-ray using the IVIS system. The VX2 liver tumor was harvested 5 minutes after intra-arterial nanoparticle injection, and a 3 mm slice was made to evaluate nanoparticle distribution using a mammography imaging system (Siemens, German). A 3 mm tumor slice was obtained in a tumor without nanoparticle injection as a control. All images were processed using ImageJ software. Fluorescence and X-ray attenuation in necrotic and peri-necrotic zones were measured using triplicate ROI selections.

Approximately half of each tumor underwent formalin-fixation and paraffin embedding to produce 5 μm sections for H&E staining to confirm necrosis, and the remainder underwent cryosection to evaluate hypericin distribution. The colocalization of hypericin and tumor necrosis was analyzed by fluorescence microscopy (Nikon, Japan).

Next, TEM was conducted to evaluate the nanoparticle distribution in cells. The VX2 hepatic tumor samples from peri-necrotic and necrotic zones were fixed by 2.5% glutaraldehyde and 1% osmium tetroxide, dehydrated by acetone, embedded by Epon812 resin, cut to 70–90 nm slices, and investigated in TEM microscope (Hitachi, Japan).

Safety evaluation *in vivo*

To evaluate the safety of Au-Hyp-NP *in vivo*, organs including heart, liver, spleen, lung, kidney, brain and pancreas were harvested at 24 h post-intravenous nanoparticle injection in treated mouse, and the same organs from a mouse without nanoparticle injection were harvested as a control. All organs were embedded in paraffin blocks, and H&E staining was conducted to evaluate tissue by histology.

Statistical analysis

Continuous variables were expressed as mean $\pm$ SD, and the differences were compared using one-way ANOVA. Statistical analysis was carried out using SPSS 20.0 (Chicago, USA). *P*-Value of less than 0.05 was considered statistically significant.

Conclusions

In this study, we have developed a novel nanoplatform simultaneously incorporating hypericin for necrosis targeting and gold for X-ray tracking, loaded into a biodegradable–biocompatible PEG-PCL carrier. The preparation method is simple and reproducible, which produced highly uniform and stable nanoparticles. Encapsulation of hypericin in biodegradable nanoparticles enables a safe nanoplatform avoiding potential toxicities of organic solvents. *In vivo* pilot studies demonstrated satisfactory necrosis targeting by Au-Hyp-NP *via* fluorescence and X-ray attenuation through both intravenous and intra-arterial administration, and nanoparticle accumulation was faster and more direct by intra-arterial administration. Thus, this strategy provides a multifunctional nano-agent with fluorescence and X-ray enhancement targeting necrosis.

This nano-agent has potential for several important contributions. Au-Hyp-NP offers the capability to assess early response to anti-tumor therapies by identifying areas of tumor necrosis. Furthermore, the presence of hypericin and gold also confer potential therapeutic functionality with photothermal and photodynamic capabilities.[22,54] With respect to cancer therapy, this strategy may prove efficacious for targeting peri-necrotic tumor areas known to harbor cancer stem cells. Finally, this nanoplatform may also be leveraged for delivery of therapeutic agents to diverse areas of necrosis, impacting broad pathophysiology such as myocardial or cerebral ischemia and cancer therapy.[6,12]

Further research will require optimization of this nanoplatform and to further characterize its *in vivo* behavior and capabilities. Nanoparticles with a size up to 60 nm have been shown to potentially demonstrate greater tumor uptake.[40] The hydrodynamic size of Au-Hyp-NP was 103.9 ± 1.7 nm, and decreasing nanoparticle size would need to balance size with loading properties. Additional *in vivo* analysis will be needed to optimize the potential theranostic profile of this nanoplatform for optimal necrosis targeting. Furthermore, the mechanisms of nanoparticle uptake and degradation for hypericin localization will be of significant interest for further study. At present, we provide proof-of-concept that encapsulation of hypericin and gold in a biocompatible nanoplatform enables necrosis affinity and imaging *in vitro* and *in vivo*. Ongoing optimization and *in vivo* studies will be the subject of future research.

Author contributions

K. Xu, O. Taratula, K. Farsad: conceptualization, supervision, project administration. X. Han, O. Taratula, A. Lorenz, A. Moses, H. Albarqi, Y. Noudeh, Q. Wu: methodology, validation, formal analysis, data curation. X. Han, K. Xu, O. Taratula: funding acquisition. X. Han, O. Taratula, K. Farsad: validation, visualization, writing – original draft, writing – review & editing.

Conflicts of interest

There are no conflicts to declare.

Acknowledgements

Notes and references

1 I. Soerjomataram, M. W. Louwman, J. G. Ribot, J. A. Roukema and J. W. Coebergh, *Breast Cancer Res. Treat.*, 2008, **107**, 309–330.

2 C. Maccalli, K. I. Rasul, M. Elawad and S. Ferrone, *Semin. Cancer Biol.*, 2018, **53**, 189–200.

3 S. Perrodin, A. Lachenmayer, M. Maurer, C. Kim-Fuchs, D. Candinas and V. Banz, *Sci. Rep.*, 2019, **9**, 13836.

4 Y. Tong, H. Yang, X. Xu, J. Ruan, M. Liang, J. Wu and B. Luo, *Cancer Sci.*, 2017, **108**, 753–762.

5 M. Varna, G. Gapihan, J. P. Feugeas, P. Ratajczak, S. Tan, I. Ferreira, C. Leboeuf, N. Setterblad, A. Duval, J. Verine, S. Germain, P. Mongiat-Artus, A. Janin and G. Bousquet, *Clin. Cancer Res.*, 2015, **21**, 916–924.

6 X. Zhang and L. Chen, *J. Cancer Res. Clin. Oncol.*, 2016, **142**, 453–463.

7 L. J. Liu and M. Schlesinger, *J. Theor. Biol.*, 2015, **380**, 1–8.

8 B. Jiang, J. Wang, Y. Ni and F. Chen, *Theranostics*, 2013, **3**, 667–676.

9 J. Li, J. Zhang, S. Yang, C. Jiang, D. Zhang, Q. Jin, Q. Wang, C. Wang, Y. Ni, Z. Yin and S. Song, *Mol. Pharm.*, 2016, **13**, 232–240.

10 X. Liu, C. Jiang, Y. Li, W. Liu, N. Yao, M. Gao, Y. Ji, D. Huang, Z. Yin, Z. Sun, Y. Ni and J. Zhang, *J. Pharm. Sci.*, 2015, **104**, 215–222.

11 H. Shao, J. Zhang, Z. Sun, F. Chen, X. Dai, Y. Li, Y. Ni and K. Xu, *Oncotarget*, 2015, **6**, 14247–14259.

12 Q. Wang, S. Yang, C. Jiang, J. Li, C. Wang, L. Chen, Q. Jin, S. Song, Y. Feng, Y. Ni, J. Zhang and Z. Yin, *Sci. Rep.*, 2016, **6**, 21341.

13 X. Qi, H. Shao, J. Zhang, Z. Sun, Y. Ni and K. Xu, *Radiol. Med.*, 2015, **120**, 213–221.

14 M. Kong, J. Zhang, C. Jiang, X. Jiang, Y. Li, M. Gao, N. Yao, D. Huang, X. Wang, Z. Fang, W. Liu, Z. Sun and Y. Ni, *J. Drug Targeting*, 2013, **21**, 604–610.

15 J. Zhu, W. Sun, J. Zhang, Y. Zhou, M. Shen, C. Peng and X. Shi, *Bioconjugate Chem.*, 2017, **28**, 2692–2697.

16 C. Spedalieri, G. P. Szekeres, S. Werner, P. Guttmann and J. Kneipp, *Nanoscale*, 2021, **13**, 968–979.

17 M. Zeisser-Labouebe, N. Lange, R. Gurny and F. Delie, *Int. J. Pharm.*, 2006, **326**, 174–181.

18 D. Long, M. Niu, L. Tan, C. Fu, X. Ren, K. Xu, H. Zhong, J. Wang, L. Li and X. Meng, *Nanoscale*, 2017, **9**, 8834–8847.

19 Q. Zhou, S. Wu, N. Gong, X. Li, J. Dou, M. Mu, X. Yu, J. Yu and P. Liang, *Nanoscale*, 2017, **9**, 11068–11076.

20 X. Han, O. Taratula, O. Taratula, K. Xu, A. St Lorenz, A. Moses, Y. Jahangiri, G. Yu and K. Farsad, *Mol. Pharm.*, 2020, **17**, 1538–1545.

21 S. Ahn, S. Y. Jung and S. J. Lee, *Molecules*, 2013, **18**, 5858–5890.

22 Z. Jendzelovska, R. Jendzelovsky, B. Kucharova and P. Fedorocko, *Front. Plant Sci.*, 2016, **7**, 560.

23 P. Miskovsky, *Curr. Drug Targets*, 2002, **3**, 55–84.

24 J. Joniova, M. Rebic, A. Strejckova, V. Huntosova, J. Stanicova, D. Jancura, P. Miskovsky and G. Bano, *Biophys. J.*, 2017, **112**, 966–975.

25 M. Van De Putte, T. Roskams, G. Bormans, A. Verbruggen and P. A. De Witte, *Int. J. Oncol.*, 2006, **28**, 655–660.

26 M. M. Cona, Y. Feng, J. Zhang, Y. Li, A. Verbruggen, R. Oyen and Y. Ni, *Drug Delivery*, 2015, **22**, 427–435.

27 L. Gao, J. Zhang, T. Ma, N. Yao, M. Gao, X. Shan, Y. Ni, H. Shao and K. Xu, *Oncotarget*, 2016, **7**, 51450–51461.

28 P. Grossen, D. Witzigmann, S. Sieber and J. Huwyler, *J. Controlled Release*, 2017, **260**, 46–60.

29 H. A. Albarqi, L. H. Wong, C. Schumann, F. Y. Sabei, T. Korzun, X. Li, M. N. Hansen, P. Dhagat, A. S. Moses, O. Taratula and O. Taratula, *ACS Nano*, 2019, **13**, 6383–6395.

30 O. Taratula, B. S. Doddapaneni, C. Schumann, X. Li, S. Bracha, M. Milovancev, A. W. G. Alani and O. Taratula, *Chem. Mater.*, 2015, **27**, 6155–6165.

31 J. Conde, A. Ambrosone, V. Sanz, Y. Hernandez, V. Marchesano, F. Tian, H. Child, C. C. Berry, M. R. Ibarra, P. V. Baptista, C. Tortiglione and J. M. de la Fuente, *ACS Nano*, 2012, **6**, 8316–8324.

32 S. Hirn, M. Semmler-Behnke, C. Schleh, A. Wenk, J. Lipka, M. Schaffler, S. Takenaka, W. Moller, G. Schmid, U. Simon and W. G. Kreyling, *Eur. J. Pharm. Biopharm.*, 2011, **77**, 407–416.

33 M. N. Vu, H. G. Kelly, A. K. Wheatley, S. Peng, E. H. Pilkington, N. A. Veldhuis, T. P. Davis, S. J. Kent and N. P. Truong, *Small*, 2020, **16**, 2002861.

34 H. Shi, M. Niu, L. Tan, T. Liu, H. Shao, C. Fu, X. Ren, T. Ma, J. Ren, L. Li, H. Liu, K. Xu, J. Wang, F. Tang and X. Meng, *Chem. Sci.*, 2015, **6**, 5016–5026.

35 L. Tan, T. Liu, C. Fu, S. Wang, S. Fu, J. Ren and X. Meng, *J. Mater. Chem. B*, 2016, **4**, 859–866.

36 S. A. Mirmalek, M. A. Azizi, E. Jangholi, S. Yadollah-Damavandi, M. A. Javidi, Y. Parsa, T. Parsa, S. A. Salimi-Tabatabaee, H. Ghasemzadeh Kolagar and R. Alizadeh-Navaei, *Cancer Cell Int.*, 2015, **16**, 3.

37 W. F. Kean and I. R. Kean, *Inflammopharmacology*, 2008, **16**, 112–125.

38 B. Xie, M. A. Stammes, P. B. van Driel, L. J. Cruz, V. T. Knol-Blankevoort, M. A. Lowik, L. Mezzanotte, I. Que, A. Chan, J. P. van den Wijngaard, M. Siebes, S. Gottschalk, D. Razansky, V. Ntziachristos, S. Keereweer, R. W. Horobin, M. Hoehn, E. L. Kaijzel, E. R. van Beek, T. J. Snoeks and C. W. Lowik, *Oncotarget*, 2015, **6**, 39036–39049.

39 C. Fang, K. Wang, C. Zeng, C. Chi, W. Shang, J. Ye, Y. Mao, Y. Fan, J. Yang, N. Xiang, N. Zeng, W. Zhu, C. Fang and J. Tian, *Sci. Rep.*, 2016, **6**, 21013.

40 X. Han, K. Xu, O. Taratula and K. Farsad, *Nanoscale*, 2019, **11**, 799–819.

41 C. G. Milross, S. L. Tucker, K. A. Mason, N. R. Hunter, L. J. Peters and L. Milas, *Acta Oncol.*, 1997, **36**, 183–189.

42 K. De Jaeger, F. M. Merlo, M. C. Kavanagh, A. W. Fyles, D. Hedley and R. P. Hill, *Int. J. Radiat. Oncol., Biol., Phys.*, 1998, **42**, 717–721.

43 J. Mao, S. Tang, D. Hong, F. Zhao, M. Niu, X. Han, J. Qi, H. Bao, Y. Jiang, C. Fu, D. Long, X. Meng and H. Su, *Nanoscale*, 2017, **9**, 3429–3439.

44 O. Chansanti, Y. Jahangiri, Y. Matsui, A. Adachi, Y. Geeratikun, J. A. Kaufman, K. J. Kolbeck, J. S. Stevens and K. Farsad, *J. Vasc. Interv. Radiol.*, 2017, **28**, 1528–1535.

45 S. Shamimi-Noori, C. F. Gonsalves and C. M. Shaw, *Semin. Intervent. Radiol.*, 2017, **34**, 145–166.

46 S. Jaju, S. K. Gupta, S. Pandey and V. Singh, *J. Cancer Res. Ther.*, 2014, **10**, 284–293.

47 M. S. Otegui, *Methods Mol. Biol.*, 2021, **2200**, 337–347.

48 D. Zukancic, E. J. A. Suys, E. H. Pilkington, A. Algarni, H. Al-Wassiti and N. P. Truong, *Pharmaceutics*, 2020, **12**, 1068.

49 X. Li, C. Schumann, H. A. Albarqi, C. J. Lee, A. W. G. Alani, S. Bracha, M. Milovancev, O. Taratula and O. Taratula, *Theranostics*, 2018, **8**, 767–784.

50 T. Duong, X. Li, B. Yang, C. Schumann, H. A. Albarqi, O. Taratula and O. Taratula, *Nanomedicine*, 2017, **13**, 955–963.

51 R. K. Dani, C. Schumann, O. Taratula and O. Taratula, *AAPS PharmSciTech*, 2014, **15**, 963–972.

52 B. W. Xie, D. Park, E. R. Van Beek, V. Blankevoort, Y. Orabi, I. Que, E. L. Kaijzel, A. Chan, P. J. Hogg and C. W. Lowik, *Cell Death Dis.*, 2013, **4**, e473.

53 O. R. Taratula, O. Taratula, X. Han, Y. Jahangiri, Y. Tomozawa, M. Horikawa, B. Uchida, H. A. Albarqi, C. Schumann, S. Bracha, T. Korzun and K. Farsad, *J. Vasc. Interv. Radiol.*, 2019, **30**, 1480–1486.

54 Y. Liu, B. M. Crawford and T. Vo-Dinh, *Immunotherapy*, 2018, **10**, 1175–1188.